Journal of Alloys and Compounds 770 (2019) 194–203

Contents lists available at ScienceDirect

Journal of Alloys and Compounds

journal homepage: http://www.elsevier.com/locate/jalcom

Effect of Al on structure and mechanical properties of Fe-Mn-Cr-Ni-Al non-equiatomic high entropy alloys with high Fe content

N.D. Stepanov [a, *], D.G. Shaysultanov [a], R.S. Chernichenko [a], M.A. Tikhonovsky [b], S.V. Zherebtsov [a]

[a] Laboratory of Bulk Nanostructured Materials, Belgorod National Research University, Belgorod, 308015, Russia
[b] National Science Center "Kharkov Institute of Physics and Technology" NAS of Ukraine, Kharkov, 61108, Ukraine

ARTICLE INFO

Article history:
Received 14 May 2018
Received in revised form
7 August 2018
Accepted 10 August 2018
Available online 16 August 2018

Keywords:
A: Metals and alloys
High entropy alloys
B: Mechanical properties
Microstructure
Phase diagrams

ABSTRACT

Microstructure and mechanical properties of the Fe-Mn-Cr-Ni-Al system non-equiatomic high entropy alloys with a different Al content (x = 0–14 at.%) were studied in the present work. The $Fe_{40}Mn_{25}Cr_{20}Ni_{15}$ alloy was composed of the face-centered cubic (fcc) matrix phase with a small amount of coarse body-centered cubic (bcc) particles. Addition of a small amount of Al (x = 2–6) resulted in an increase in the fraction of the bcc phase to 26% and the formation of fine B2 precipitates within the bcc phase. At higher amounts of Al (x = 10 and x = 14) the microstructure consisted of coarse bcc matrix grains with the B2 precipitates inside. The alloys tend to become stronger with an increase in the Al content from 0 to 10 at.%; further increase in Al concentration did not influence strength considerably. The alloys exhibited pronounced softening with an increase in testing temperature from 25 to 400 °C–600 °C. Ductility of the alloys was high enough (>50%) at all temperatures. A quasi-binary $Fe_{40}Mn_{25}Cr_{20}Ni_{15}$-Al phase diagram was constructed using a ThermoCalc software and a TCHEA2 database; reasonable agreement between the experimental and predicted phase compositions of the alloys was obtained. It was suggested that an addition of the strong bcc-stabilizing and compound-forming Al to a bcc-prone $Fe_{40}Mn_{25}Cr_{20}Ni_{15}$ alloy is beneficial for the development of the alloys with the disordered bcc matrix and the embedded B2 precipitates having attractive mechanical properties.

1. Introduction

The so-called high entropy alloys (HEAs) represent a new class of metallic alloys with promising properties suitable for advanced applications [1–3]. Unlike most of the traditional metallic alloys, HEAs have extremely complex chemical composition – according to the original definition, they should be composed of at least 5 principal elements taken in approximately equiatomic concentrations (5–35 at.%) [4]. Due to the chemical complexity, these alloys were supposed to possess unique structures and properties unattainable in conventional alloys [2,5]. Indeed, some of the reported HEAs demonstrated remarkable properties like high strength (at room or elevated temperatures), eminent toughness, wear resistance and so on [6–19]. However, the design of HEAs with a good combination of properties suitable for practical applications still remains an unsolved problem.

Although initially a strong emphasis has been made on alloys with a single solid solution phase structure [1,4], it is well accepted that the presence of two (and sometimes more) phases is beneficial for the obtaining the best combination of mechanical properties [20]. Like conventional metallic materials, alloys with the solid solution matrix phase strengthened by precipitates of a second phase with, probably, an ordered structure, are likely to possess a good combination of strength (including that at high temperatures) and ductility [21,22]. This approach has been recently developed for CoCrFeNi(Mn) alloys with an face-centered cubic (fcc) matrix [23–27]. For instance, alloying of a single fcc phase CoCrFeNi alloy with 4 at.% of Al and 2 at.% of Ti together with a proper heat treatment has promoted strong precipitation strengthening by $L1_2$ particles [28]. As a result, the alloy had the ultimate tensile strength of ~1100 MPa and elongation of ~40%.

Abilities of the alloys with a bcc structure to precipitation hardening are much less studied [29]. It is generally believed that

* Corresponding author. Laboratory of Bulk Nanostructured Materials, Belgorod State University, Pobeda 85, Belgorod, 308015, Russia.
E-mail addresses: stepanov@bsu.edu.ru, stepanov.nikita@icloud.com (N.D. Stepanov).

https://doi.org/10.1016/j.jallcom.2018.08.093
0925-8388/

the body-centered cubic (bcc) HEAs are stronger but less ductile in comparison with the fcc counterparts, yet there are some examples of highly ductile bcc alloys [1,30,31]. There are several elements which can turn the fcc structure of the Co-Cr-Fe-Ni-(Mn) system alloys into the bcc one. One of these elements is Al [32–42]. However, Al is also a strong intermetallic compound former, especially when added together with Ni. For instance, an addition of Al to an equiatomic CoCrFeMnNi alloy results in a gradual transformation of an fcc-based structure to a bcc-based structure through a mixture of the fcc and bcc phases [43]. This transformation is accompanied by a continuous increase in strength. Nevertheless, it has been found that the bcc-based structure is composed of an ordered B2 matrix phase with disordered bcc precipitates. The alloys with such structure are brittle even in compression.

Recently, several alloys of an Al-Co-Cr-Fe-Ni-Mn system which have the bcc matrix phase strengthened by the B2 or $L2_1$ phase particles were reported [44–48]. These alloys have been found to possess reasonable ductility in tension and rather attractive strength at high temperatures. For example, a $Fe_{36}Mn_{21}Cr_{18}Ni_{15}Al_{10}$ alloy was found to exhibit the ultimate tensile strength of 880 MPa at room temperature which even increased slightly at 400 °C [44]. However at higher temperatures (500–600 °C) pronounced softening occurred. A better understanding of the composition-structure-properties relationship is needed to improve properties of such alloys further. For instance, it is not completely clear at the moment why the disordered bcc matrix with the B2 precipitates can be obtained in certain alloys, what amount of Al is required to produce such structures etc.

In the present work, we have studied the structure and mechanical properties of a series of alloys of the Fe-Mn-Cr-Ni-Al system with different Al contents based on a non-equiatomic $Fe_{40}Mn_{25}Cr_{20}Ni_{15}$ alloy which includes the previously reported $Fe_{36}Mn_{21}Cr_{18}Ni_{15}Al_{10}$ alloy [44]. Two main aims were pursued: (i) to gain a better understanding of the bcc/B2 structure formation in the Fe-Mn-Cr-Ni-Al high entropy alloys; (ii) to estimate how the phase evolution affects mechanical properties in such alloys, including that at high temperatures.

2. Materials and methods

Alloys with the nominal compositions of $(Fe_{40}Mn_{25}Cr_{20}Ni_{15})_{100-x}Al_x$ (x = 0; 2; 6; 10; 14; the numbers indicate the atomic percentage (at. %)) were produced by vacuum arc melting. For simplicity, the alloys will hereafter be designated by the percentage of Al (x = 6 alloy for example). High-purity (at least 99.9%) powders of the constitutive elements were used as the starting materials. The produced ingots had dimensions of ~10 × 15 × 60 mm^3. The ingots were remelted 5 times to ensure chemical homogeneity. SEM-EDX analysis showed that the actual chemical composition of the alloys closely corresponded to nominal ones (Table 1). The specimens for microstructural characterization and mechanical testing were cut from the produced ingots using an electric discharge machine.

Microstructure and phase composition of the alloys in the as-cast condition were studied using X-ray diffraction (XRD), scanning (SEM) and transmission (TEM) electron microscopy techniques. XRD analysis was performed using a RIGAKU diffractometer with Cu Kα radiation. Samples for SEM observations were prepared by careful mechanical polishing. SEM investigations were performed using an FEI Quanta 600 field emission gun (FEG) microscope equipped with a back-scattered electron (BSE) and an energy-dispersive (EDS) detectors. Samples for TEM analysis were prepared by the conventional twin-jet electro-polishing of mechanically pre-thinned to 100 μm foils, in a mixture of 95% C_2H_5OH and 5% $HClO_4$ at the 27 V potential. TEM investigations were performed using a JEOL JEM-2100 microscope equipped with an EDS detector at an accelerating voltage of 200 kV. The volume fractions of different phases were measured from SEM-BSE images using a Digimizer Image Analysis Software.

Compression mechanical tests were performed using samples of the alloys in the as-cast condition. The testing was performed on an Instron machine equipped with a radial heating furnace. Rectangular specimens with dimensions of 7 × 5 × 5 mm^3 were used. The testing was performed at room (25 °C) and elevated (400 or 600 °C) temperatures at an initial strain rate of 10^{-4} s^{-1} until 50% height reduction. For the elevated temperature compressions, the specimens were placed in the preheated to the testing temperatures furnace and held for ≈10 min to equilibrate the temperature prior to the testing. The temperature of the specimens was controlled by a thermocouple attached to a side surface of the specimens.

Equilibrium phase diagrams were constructed using a Thermo-Calc (version 2017a) software employing a TCHEA2 (high-entropy alloys) database.

3. Results

3.1. Structure of the alloys

Fig. 1 shows XRD patterns which illustrate the effect of the Al

Table 1
The chemical composition of the structural constituents of the $(Fe_{40}Mn_{25}Cr_{20}Ni_{15})_{100-x}Al_x$ alloys with different Al concentration (x) as determined by SEM-EDS. Typical regions for the analysis are shown in Fig. 1.

Element at.%		Fe	Mn	Cr	Ni	Al
№	Structural constituent					
x = 0						
1	Matrix	38.9	25.9	19.8	15.4	–
2	Particles	40.9	20.1	32.5	6.5	–
Actual composition		39.2	25.5	20.1	15.2	–
x = 2						
1	Matrix	38.1	24.2	19.5	15.7	2.5
2	Particles	40.5	20.2	28.7	8.2	2.4
Actual composition		39.0	23.3	20.1	15.1	2.5
x = 6						
1	Matrix	37.8	22.8	17.9	15.5	6.0
2	Particles	36.7	23.5	19.1	13.9	6.8
Actual composition		37.7	22.9	18.5	14.4	6.5
x = 10						
Actual composition		36.5	21.0	18.3	14.3	10.0
x = 14						
Actual composition		34.6	20.3	17.2	13.4	14.7

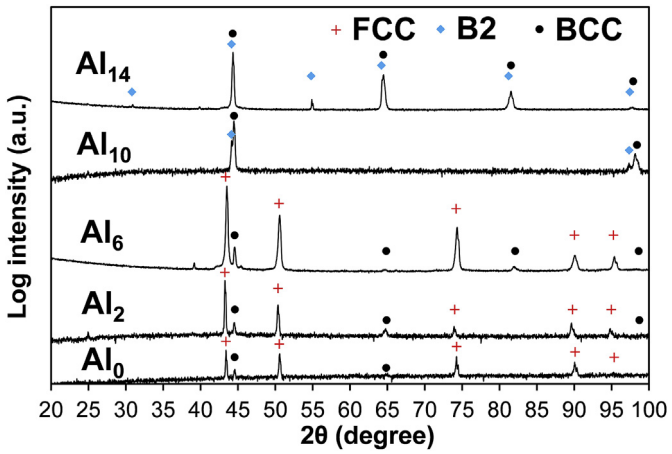

Fig. 1. XRD patterns of the $(Fe_{40}Mn_{25}Cr_{20}Ni_{15})_{100-x}Al_x$ alloys with different Al concentrations.

content in a range 0–14 at.% on the phase composition of the $(Fe_{40}Mn_{25}Cr_{20}Ni_{15})_{100-x}Al_x$ alloys. The alloy without Al (x = 0) was composed of a main fcc phase and a minor bcc phase. The lattice parameters of the fcc and bcc phases were 0.361 and 0.288 nm, respectively. An addition of Al resulted in a gradual decrease in the intensity of the fcc peaks and, vice versa, an increase in the intensity of the bcc maximums. However, the fcc phase remained dominant at the Al percentage up to 6 at.%. An increase in the Al concentrations above 6 at.% had not resulted in noticeable changes of the lattice parameters of the fcc and bcc phases. At yet higher Al contents, i.e. x = 10 or x = 14, the fcc phase was not found. However, a strong splitting of the bcc peaks suggested that the alloys were composed of two bcc phases with different lattice parameters – 0.288–0.289 and 0.290 nm, respectively. Note that the characteristic B2 superlattice reflections were detected for only one of the bcc phases.

Fig. 2 shows SEM-BSE images of the $(Fe_{40}Mn_{25}Cr_{20}Ni_{15})_{100-x}Al_x$ alloys microstructure depending on the Al content. The chemical compositions of the constitutive phases are summarized in Table 1. The alloy without Al (Fig. 2a) was composed of two phases: the matrix one (#1 in Fig. 2a) had a composition close to the nominal one, and the darker second phase particles (#2) were found to be enriched with Cr and depleted of Mn and Ni (Table 1). Note that Cr is a well-known bcc stabilizer while Mn and Ni are fcc-stabilizing elements. The second phase particles had a complex irregular, often elongated shape and a thickness of 1–5 μm. A volume fraction of the second phase was 6%. An average size of the matrix grains was 75 μm.

With an increase in the Al content to x = 2 (Fig. 2b) or x = 6 (Fig. 2c) microstructure of the alloys remained quite similar to that of the Al-free alloy. However, one can clearly see that the volume fraction of the second phase particles increased with an increase in the Al content to 12% (2 at.% Al) or 26% (6 at.% Al). The second phase particles in the x = 2 alloy also became coarser attaining the thickness of 4–10 μm. In the x = 6 alloy, the thickness of the second phase particles was close to that in the Al-free alloy, but they started to form a continuous network with mostly elongated cells. A closer look at the structure of the alloy (insert in Fig. 2c) revealed some finer, cuboidal or rectangular particles inside the coarse second phase particles. Similarly to the Al-free alloy, the coarse particles were enriched with Cr and depleted of Mn and Ni (Table 1).

Drastic changes in microstructure were observed when the Al content increased to x = 10 and x = 14 (Fig. 2d and e). In both alloys, low magnification images demonstrated apparently a single phase granular structure with a grain size of ~150–200 μm. However, higher magnification inserts clearly showed the presence of precipitates inside the coarse matrix grains. In both alloys these precipitates had a submicron size; however, they tend to have a cuboidal morphology in the alloy with 10 at.% of Al, and a spherical one – in the alloy with 14 at.% of Al. The chemical composition of these precipitates could not be determined by SEM-EDS analysis reliably because of a small size.

To gain more detailed information on the $(Fe_{40}Mn_{25}Cr_{20}Ni_{15})_{100-x}Al_x$ alloys structure, additional TEM studies were performed (Fig. 3). The Al-free (x = 0) alloy was composed of the matrix (#1, Fig. 3a) and coarse second phase particles. Selected area diffraction patterns (SAEDs) demonstrated that the matrix has an fcc structure while the second phase particles had a bcc structure. Moreover, numerous very fine precipitates inside the second phase particles can be recognized. The crystal structure and chemical composition of these particles could not be determined via SAEDs/EDS because of a very small (~3 nm) size.

TEM images of the alloys with a higher Al content (x = 2 and x = 6) demonstrated rather similar structures of the fcc matrix phase (#1 in Fig. 3b and c) with the bcc second phase particles (#2). Moreover, in both alloys cuboidal precipitates were observed inside the bcc phase. Analysis of SAEDs had revealed that these precipitates had a B2 structure. Examination of the chemical composition of the cuboidal precipitates in the alloy with x = 6 has demonstrated that they are enriched with Al and Ni. TEM-EDS chemical analysis of other phases showed results pretty similar to those obtained by SEM-EDS (Table 1).

Quite a different structure was observed in the alloys with a high Al content (x = 10 (Fig. 3d) and x = 14 (Fig. 3e)). The microstructure was found to be composed of the bcc matrix phase with the embedded B2 precipitates (which are clearly visible in the corresponding dark-field inserts). The precipitates had cuboidal or spherical shapes in the x = 10 or the x = 14 alloys, respectively. The change in the morphology of the precipitates can potentially be attributed to the difference in the lattice misfits between bcc matrix and B2 precipitates in the two alloys [46]. An average size of the B2 precipitates was 160 nm or 190 nm in the x = 10 or x = 14 alloys, respectively. In both alloys, the B2 precipitates were enriched with Al (16–18 at.%) and Ni (20–23 at.%), while the matrix was primarily composed of Fe (43–47 at.%) and Cr (22–23 at.%). Mn was uniformly distributed between the phases.

3.2. Mechanical properties

Fig. 4 presents stress-strain curves obtained during compression testing of the $(Fe_{40}Mn_{25}Cr_{20}Ni_{15})_{100-x}Al_x$ alloys with different Al concentrations at room or elevated temperatures (25, 400, or 600 °C). Increasing slope of the elastic part of the curves suggested growing elastic modulus of the alloys with an increase in the Al content; yet the testing conditions (compression) did not allow an accurate measurement of the elastic moduli. Nevertheless, it seems that the difference in the elastic moduli of the alloys was less significant at 600 °C in comparison with that at room temperature or 400 °C. Note that an increase in the elastic modulus with Al concentration in similar alloys at room temperature has already been reported [49].

Mechanical behavior of the alloys at room temperature after yielding was associated with a prolonged hardening stage (Fig. 4a). The slope of the curves at the strengthening stage was similar for all the alloys with different Al concentrations. Also, all the alloys can be compressed without fracture to 50% reduction (both at room and elevated temperatures). However, the yield strength of the alloys at room temperature showed a pronounced dependence on the Al

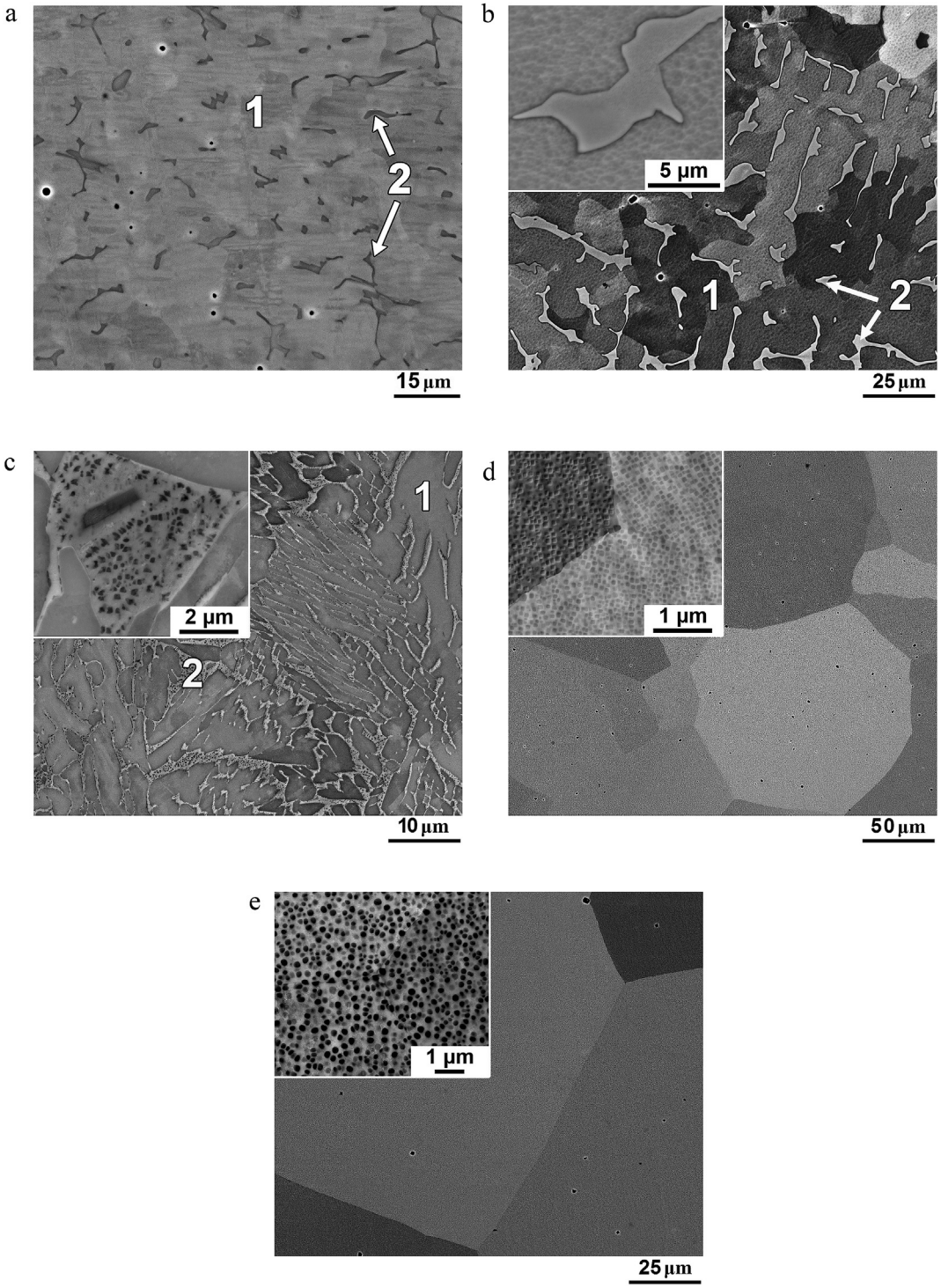

Fig. 2. SEM-BSE images of the $(Fe_{40}Mn_{25}Cr_{20}Ni_{15})_{100-x}Al_x$ alloys with different Al concentration (x): a – x = 0; b – x = 2; c – x = 6; d – x = 10; e – x = 14. Numbers on the images indicate typical structural constituents, determined by the chemical analysis (see Table 1).

concentration (Fig. 5) almost linearly increasing for Al from 0 to 10 at.% and then slightly decreased at x = 14.

At 400 °C the alloys demonstrated mechanical behavior very similar to that at room temperature. Note that the yield strength values were only slightly lower in comparison to those at room temperature (Fig. 5). However, a pronounced hardening stage was observed in the alloys with a low Al content only while the alloys with a high Al concentration (10 or 14 at.%) showed rather weak work hardening. Further increase in temperature to 600 °C resulted in more pronounced changes. The yield strength of the alloys dropped significantly (Fig. 5) in comparison to 400 °C or 600 °C with an increase in the Al concentration. Interestingly, the alloys with a high content of Al (10 or 14 at.%) demonstrated nearly steady-state flow stage soon after the yielding whereas the alloys which contain less Al (0 or 2 at.%) showed continuous strengthening. As the result, the flow stress of the x = 2 alloy became higher

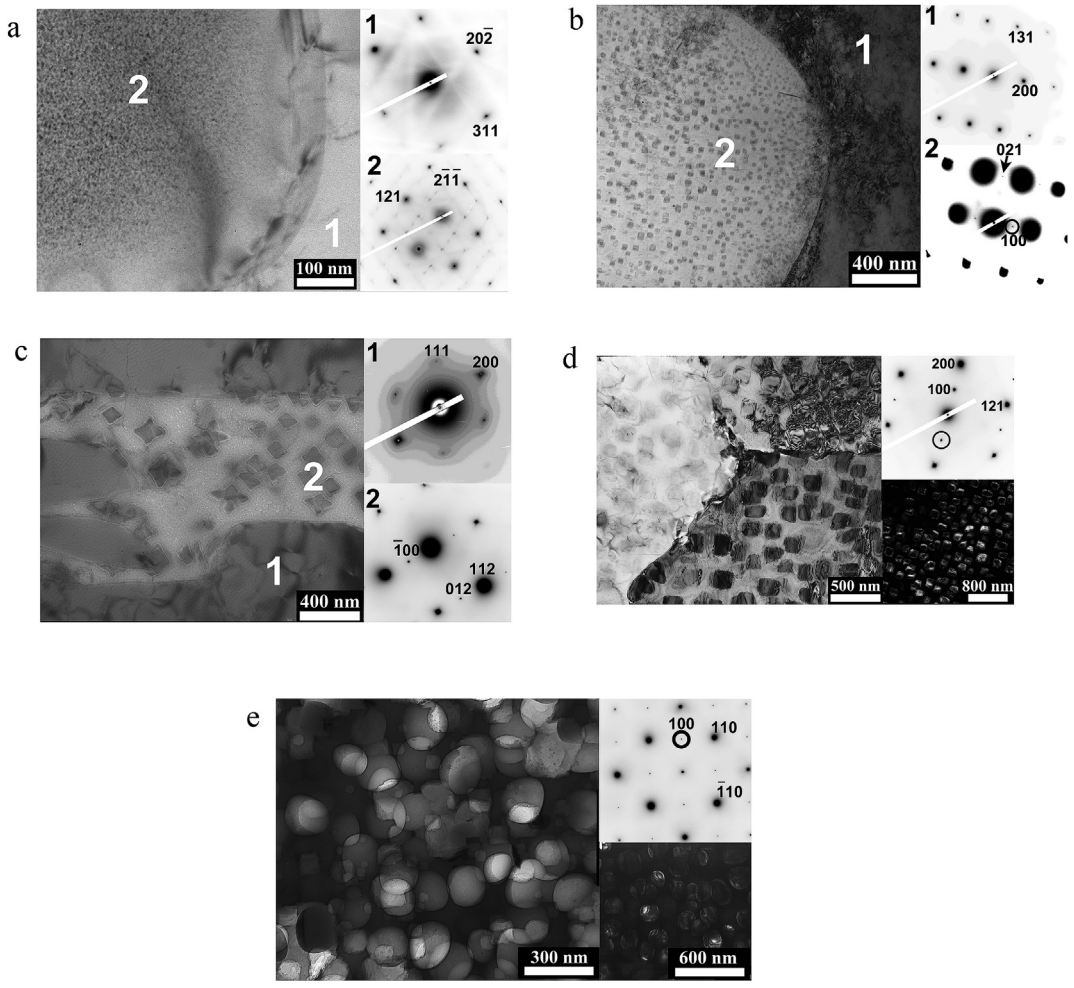

Fig. 3. TEM bright-field images of the Fe-Mn-Cr-Ni-Al alloys with different Al concentrations (x): a – x = 0; b – x = 2; c – x = 6; d – x = 10; e – x = 14; Selected area diffraction patterns of the constitutive phases and dark-field images of the B2 phase (d, e) are shown in inserts.

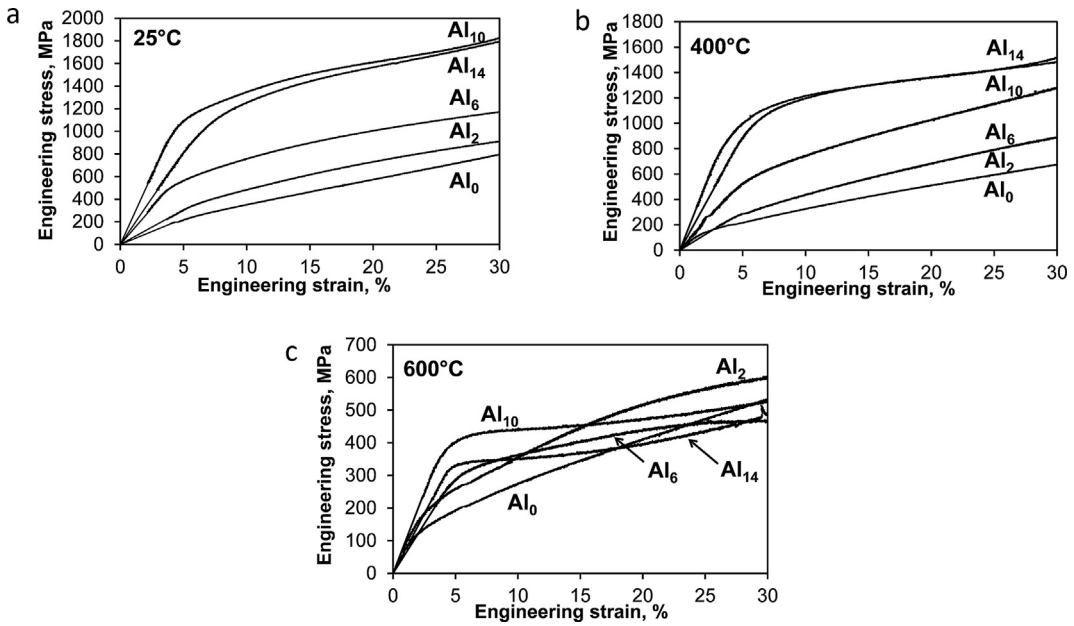

Fig. 4. Compression stress-strain curves of the $(Fe_{40}Mn_{25}Cr_{20}Ni_{15})_{100-x}Al_x$ alloys with different Al concentrations (x) obtained at different temperatures: a - 25 °C, b - 400 °C, d - 600 °C.

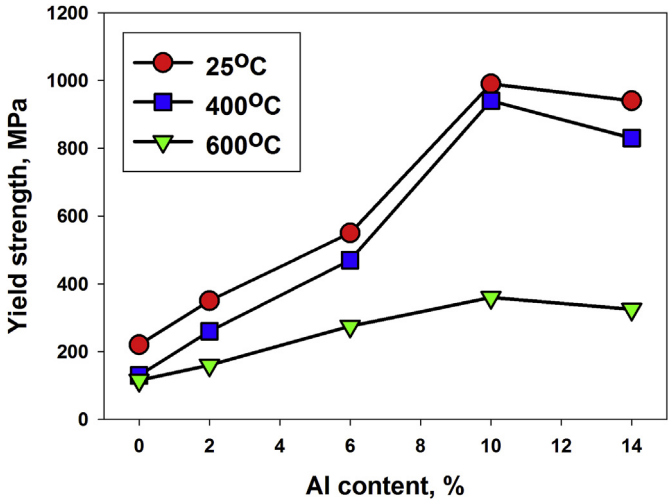

Fig. 5. Dependence of the compression yield strength of the $(Fe_{40}Mn_{25}Cr_{20}Ni_{15})_{100-x}Al_x$ alloys with different Al concentrations (x) obtained at 25 °C, 400 °C, or 600 °C.

than those of the rest of the alloys after ≈15% of compression deformation.

3.3. Phase diagrams

In order to gain a better understanding of the phase equilibrium in the experimental alloys, we have produced a quasi-binary $Fe_{40}Mn_{25}Cr_{20}Ni_{15}$–Al phase diagram using the ThermoCalc software (Fig. 6a). For the sake of comparison, a well-studied CoCrFeMnNi-Al [43] system phase diagram was also produced (Fig. 6b). The $Fe_{40}Mn_{25}Cr_{20}Ni_{15}$ alloy was expected to solidify starting from a bcc phase; an fcc phase appeared at the latter stages of solidification (Fig. 6a). After solidification, the alloy was composed of a mixture of the fcc and bcc phases; a tiny single fcc phase field was observed at lower temperatures. Below ≈1150 °C, a prolonged fcc+sigma phases field was expected. An addition of Al resulted in: (i) A gradual increase in the liquidus temperature of the alloys, associated primary with some expansion of a liquid+bcc field. (ii) The suppression of the fcc phase, for example, an alloy started to solidify with the bcc phase solely when the Al content was higher than ≈4%, and the single fcc field disappeared when the Al content was above ≈1%. Yet, in a low-temperature part of the phase diagram the fcc phase was presented in multiphase fields at the Al concentrations up to ≈11%. (iii) The solvus temperature of the sigma phase pronouncedly decreased from ≈1150 °C to ≈1000 °C when the Al content increased from 0 to ≈6%. (iv) The B2 phase precipitation started when the Al concentration reached ≈6 at.%; the solvus temperature of the B2 phase gradually increased with an increase in the Al concentration.

The quasi-binary CoCrFeMnNi-Al phase diagram (Fig. 6b) showed significant differences from that for the $Fe_{40}Mn_{25}Cr_{20}Ni_{15}$–Al system (Fig. 6a). The equiatomic CoCrFeMnNi alloy solidified through a single fcc phase, and a sigma phase was expected to precipitate starting from ≈800 °C. The predicted sigma phase precipitation was in agreement with some recent reports [50,51]. With an increase in the Al concentration to ≈1.5 at.%, the B2 phase started to precipitate first from the fcc primary phase. The solvus temperature of the B2 phase quickly increased with a further increase in the Al concentration. At the Al percentage of ≈6 at.%, the bcc phase appeared at the solidification stage. Its fraction continuously increased, and at the Al concentration of ≈11% the solidification occurred completely through the bcc (+B2) phase(s) and the fcc phase occurred through a solid state reaction, while at ≈17 at.% Al the fcc phase disappeared in the alloys (not shown in Fig. 6b) completely.

4. Discussion

The obtained information suggested that the addition of Al to the $Fe_{40}Mn_{25}Ni_{20}Cr_{15}$ alloy resulted in: (i) a gradual transformation of the (mostly) fcc structure into the fully bcc one and (ii) the ordered B2 precipitates formation (Figs. 1–3). The stability of different phases, including the bcc and fcc ones, in 3d transition metals HEAs is well studied. It was found that the valence electron concentration parameter (*VEC*, $VEC = \Sigma\, c_i VEC_i$, where c_i and VEC_i are the atomic concentration and the valence electron concentration of the *i* element, respectively) can be used to predict the fcc and bcc phases formation in HEAs. According to the statistical analysis conducted by Guo et al. the fcc phase(s) form in HEAs with $VEC > 8$, the bcc phase(s) form at $VEC < 6.87$ and both the fcc and bcc phases coexist in the alloys with the *VEC* values between 6.87 and 8.0; i.e. a decrease in VEC favors the bcc structures [52].

Our results are in reasonable agreement with these predictions; the *VEC* parameter of the studied alloys gradually decreased from 7.65 to 7.0 with an increase in the Al concentration from 0 to 14 at.% because Al has low VEC_i (3). The *VEC* values of the alloys with the fcc+bcc structure (x = 0–6) were 7.37–7.65, i.e. fell in the range of VEC for fcc+bcc mixtures, while the solely bcc alloys (x = 10–14) have *VEC* of 7.00–7.19. These values were slightly higher than the threshold values for the bcc to fcc+bcc structures transition (6.87). Possibly, this discrepancy can be attributed to a large amount of Mn in the studied alloys [52]. However, note that the recent analysis of Al-Co-Cr-Fe-Ni HEAs with different ratios of Co, Cr, Fe, and Ni has revealed a transition from the bcc+fcc to the bcc+B2 structure at

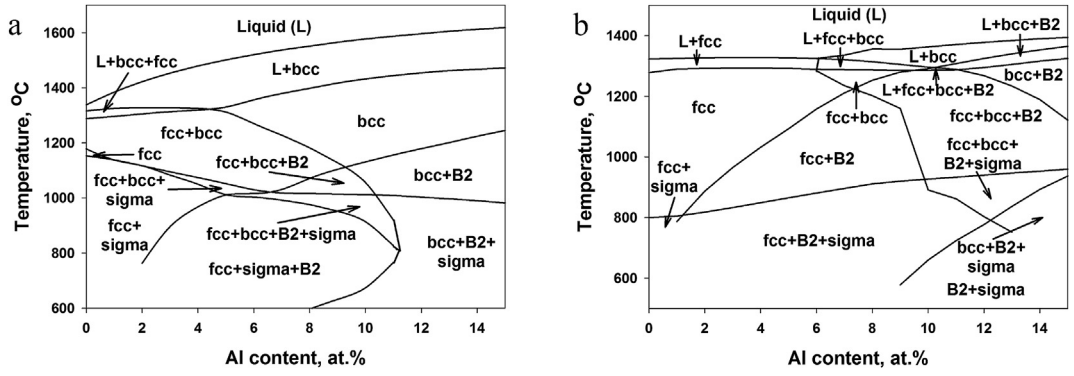

Fig. 6. Quasi-binary phase diagrams: a - the $Fe_{40}Mn_{25}Cr_{20}Ni_{15}$–Al system and b - CoCrFeMnNi-Al system.

VEC<7.35 [46], i.e. very similar to our results. In turn, the B2 Al, Ni-rich precipitates formation in Al-containing alloys can be attributed to highly negative formation enthalpy of intermetallics compounds (ΔH_f) in the AlNi pair. An extensive analysis by Troparevsky et al. have demonstrated that the corresponding ΔH_f value equaled to −677 meV/atom [53].

Eventually, an addition of Al to 3d transition metals HEAs has a twofold effect: (i) stabilization of the bcc structure due to a decrease in *VEC*; (ii) the Al, Ni-rich intermetallics formation due to their low formation enthalpy [32]. In the studied series of alloys, the starting $Fe_{40}Mn_{25}Cr_{20}Ni_{15}$ alloy was already prone to the bcc phase formation (Fig. 1). Therefore, relatively small amounts of Al (10 at.%) were required to a complete turn to the bcc structure. This amount of Al resulted in the formation of B2 Al, Ni-rich phase, yet only as precipitates in the disordered bcc matrix. When Al was added to entirely fcc equiatomic alloys, like CoCrFeNi or CoCrFeMnNi (the corresponding *VEC* values were 8.25 or 8.0, respectively [54]), a much higher amount of Al was required to form the entirely bcc structure. For example, more than 16 at.% of Al should be added to the CoCrFeMnNi alloy to make it completely bcc [43]. Apparently, this amount of Al strongly promoted the formation of intermetallic phases, and, as the result, the CoCrFeMnNi alloys with a high amount of Al have the ordered B2 matrix.

The comparison of the experimentally obtained data on the structure of the $(Fe_{40}Mn_{25}Cr_{20}Ni_{15})_{100-x}Al_x$ alloys (Figs. 1–3) and the calculated phase diagram (Fig. 6a) showed rather a close resemblance. Please note that the experimental alloys were studied in a non-equilibrium as-cast condition and therefore a direct comparison between the experimental and calculated results is not quite correct. Nevertheless, it seems that the transition between the fcc+bcc and bcc structures with an increase in Al concentration is rather accurately predicted; in high-temperature phase fields (not including the sigma phase) this transition is expected at ≈9–10 at.% of Al. However, there is also some discrepancy with the experimental results. For example, the B2 particles are expected to precipitate at a relatively high Al concentration (>6 at.%), although they were experimentally observed already in the alloy with 2 at.% of Al (Fig. 3b). This can be associated with some difference in the predicted chemical composition of the B2 phase (which is close to the binary NiAl compound) in comparison with the experimental alloys where the total concentration of Al and Ni in the B2 particles was ~35–40 at.%.

The following sequence of the phase transformations in the experimental alloys during cooling from the melt can be expected from the phase diagram (Fig. 6a). All alloys start to solidify through single bcc phase, yet in the alloys with low Al concentration (x = 0–6) the fcc phase appears at the latter stages of solidification and consumes most of the initial bcc phase. The irregular appearance of the bcc phase in the (x = 0–6) alloys (Fig. 2 a–c) confirms that the fcc+bcc mixture was produced during solidification. During further cooling, fine unidentified (x = 0 alloy (Fig. 3a)) or Al, Ni-rich B2 (x = 2–6 alloys (Fig. 3b and c)) precipitates appear in the as-solidified bcc phase by solid-state reaction. Most probably, this is due to the highly non-equilibrium chemical composition of the as-solidified bcc phase. Meanwhile in the alloys with high Al concentration (x = 10–14) the solidification finishes with the sole bcc phase (Fig. 2d and e), and the fine B2 precipitates are produced during further cooling (Fig. 3d and e).

A very important aspect of the constructed phase diagram (Fig. 6a) is the presence of the large single bcc phase field followed by the lower temperature dual-phase bcc+B2 phase field in the alloys with a high Al content (≥10 at.%). This type of the phase diagram suggests wide opportunities for the microstructure control, i.e. solution heat treatment in the single phase field with a subsequent aging treatment at lower temperatures to attain a high strengthening effect due to the formation of precipitating particles with a required size and volume fraction. For example, it was revealed that duplex B2 precipitates can be introduced into ferritic (bcc) Fe-Cr-Ni-Al steel by proper heat treatment; such duplex precipitates had a beneficial effect on room temperature mechanical properties [55]. In the case of the investigated $(Fe_{40}Mn_{25}Cr_{20}Ni_{15})_{100-x}Al_x$ alloys, the as-cast dual phase bcc/B2 structure of the x = 10 alloy can be maintained after annealing at 1200 °C for 24 h [44]. Only microhardness measurements were performed after annealing, but they did not suggest significant variations in other mechanical properties. However, a considerable decrease in microhardness was found in the alloy after annealing at 1000 °C for 24 h. Softening was associated with the formation of fcc phase [44]. Therefore, future studies are required to experimentally establish the effect of heat treatment on structure and mechanical properties of the alloys and to select the best possible processing routes.

Contrary to the $Fe_{40}Mn_{25}Cr_{20}Ni_{15}$–Al system, in the CoCrFeMnNi-Al alloys with a low Al content the only expected solidification product is the fcc phase; the bcc phase is expected to appear at Al concentrations of ≥6 at.% only, and the fcc phase disappears completely at 17 at.% of Al (Fig. 6b). The predicted phase diagram of the CoCrFeMnNi-Al system is in good agreement with experimental data [43]. In the as-cast condition, the fcc structure was found in the alloys with the Al fraction <8 at.%, the fcc+bcc structure was observed at 8–16 at.% of Al, and the single-phase bcc structure was obtained at a yet higher Al concentration. It should be noted that a similar transition from the fcc phase to the bcc (B2) one as the primary solidification product was demonstrated both experimentally and computationally in other systems like Al_xCoCuFeNi$_2$ [42]. Moreover, according to the phase diagram, in the alloys with the Al content above 11 at.% the bcc+B2 mixture forms already during solidification. Therefore the possibilities to control the B2 phase fraction and morphology via a heat treatment are limited.

The disordered bcc matrix phase apparently benefits ductility of the studied $(Fe_{40}Mn_{25}Cr_{20}Ni_{15})_{100-x}Al_x$ alloys; all of them have demonstrated high compression ductility (>50%) in the temperature interval 25–600 °C (Fig. 4). The chemical and phase compositions of the alloys have not affected their ductility. Nevertheless one must keep in mind that uniaxial compression is a “soft” testing scheme; while tensile ductility of the alloys may be much lower. For instance, the x = 10 alloy has earlier been demonstrated the elongation to fracture of only 2.5% at room temperature [44]. Therefore tensile ductility of the alloys will probably be more sensitive to their composition and/or structure.

Meanwhile the yield strength of the alloys was significantly affected by their chemical composition, as the yield strength increased from ~200 MPa to ~1000 MPa at room temperature with an increase in the Al content (Fig. 5). It is already well established that an increase in the fraction of a “hard” bcc(+B2) phase(s) results in pronounced strengthening of 3d transition metals HEAs [32,33,43,56]. The dependence of the yield strength of the experimental Fe-Mn-Cr-Ni-Al alloys as a function of the bcc(+B2) phase(s) fraction is shown in Fig. 7. The studied alloys can clearly be grouped into two types with respect to the bcc(+B2) phase(s) fraction: the first type contains a relatively small amount of the bcc phase(s) − 5.6–26.0% (x = 0–6 alloys); the second type is entirely composed of the bcc+B2 structure (x = 10–14 alloys). For the first group of the alloys, a linear relationship between the yield strength and the bcc(+B2) phases fraction is found (Fig. 5). This type of dependence suggests a composite-like behavior of the alloys composed of the softer fcc phase and the harder bcc(+B2) phase(s) and is in agreement with previous reports [33,43].

The investigated series of alloys covers only limited set of

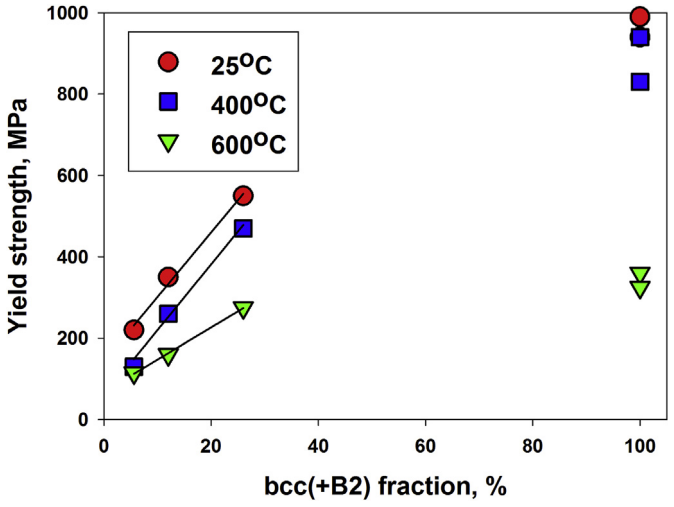

Fig. 7. Dependence of the yield strength of the $(Fe_{40}Mn_{25}Cr_{20}Ni_{15})_{100-x}Al_x$ alloys with different Al concentrations on a fraction of bcc(+B2) phases.

possible bcc amounts, yet the approximation of the dependencies obtained for the x = 0–6 alloys to a fully bcc+B2 structure (x = 10–14 alloys) gives ~2 times higher yield strength values than that of the experimental alloys. This finding suggests that the linear relationship between the strength and the fraction of the bcc phase(s) is valid for a certain range of the bcc(+B2) fraction only. Linear dependencies obtained for the relatively low bcc(+B2) fractions suggest that the maximum strength level of the experimental alloys is reached at ≈42–53% of the bcc(+B2) phase(s); i.e. when the fraction of the fcc and bcc phases are approximately equal. It might be suggested that when the fcc phase is dominant, plastic deformation occurs mainly in this softer phase, while the bcc(+B2) phase(s) serve as a reinforcement. However, when the alloys have the bcc-based structure, it became strongly involved in the plastic flow and the much softer fcc phase does not provide any effective strengthening. In this case, probably, the strength of the alloys would be strongly dependent on the fraction and size of the B2 phase inside the bcc matrix. For instance, the strength of the x = 14 alloy is slightly lower than that of the x = 10 alloy (Fig. 5) most probably due to coarser B2 precipitates (Fig. 3d and e).

Data obtained in the current study also suggests that strengthening by the bcc(+B2) phase(s) is strongly dependent on testing temperature. For example, one can compare the slope dependence of the yield strength on the bcc(+B2) fraction (linear part) at 25 °C/400 °C or 600 °C (Fig. 7). Apparently, the strengthening effect is almost identical at 25 °C or 400 °C and is much less pronounced at 600 °C. It is well accepted that generally the bcc metals and alloys soften faster with increasing temperature than the fcc ones [57]. Therefore, it is not surprising that the drop of strength with an increase in testing temperature becomes much more pronounced as the Al concentration (and the bcc phase fraction) increases (Fig. 5). Note that similar behavior has been already reported for 3d transition metals HEAs; for instance, $Al_xCoCuCrFeNi$ alloys with a high Al content softened faster at elevated temperatures [58].

To sum up, the present study has demonstrated that an addition of Al to the 3d transition metals HEAs which are already prone to the bcc phase formation results in a superalloy-like microstructure composed of the bcc matrix with the embedded B2 precipitates. Such alloys demonstrate high strength together with reasonable ductility and therefore can be considered as promising structural materials. ThermoCalc calculations can be used to predict the phase composition of these alloys and therefore tailor their chemical and phase compositions, microstructures, and properties. In particular, additional efforts are required to develop alloys with higher resistance to softening at temperatures of 600 °C and above.

5. Conclusions

In this work, microstructure and mechanical properties of the $(Fe_{40}Mn_{25}Cr_{20}Ni_{15})_{100-x}Al_x$ high entropy alloys with a different Al content (x = 0–14 at.%) after vacuum arc melting and casting were studied. The following conclusions were drawn:

1) The $Fe_{40}Mn_{25}Cr_{20}Ni_{15}$ alloy was composed of the fcc matrix phase with a small amount (6 vol.%) of coarse bcc particles containing nanoscale precipitates of an unidentified structure. Alloying with small amounts of Al (x = 2 and x = 6) resulted in an increase in the fraction of the bcc phase to 12% and 26%, respectively. Inside the bcc phase, fine B2 precipitates were found. The bcc phase was enriched with Fe and Cr, and the B2 precipitates - with Ni and Al. Alloys with higher amounts of Al (x = 10 and x = 14) were composed of coarse bcc matrix grains with the B2 precipitates inside.
2) The equilibrium quasi-binary $Fe_{40}Mn_{25}Cr_{20}Ni_{15}$-Al phase diagram was constructed using a ThermoCalc software and TCHEA2 database and used to analyze the effect of Al on the phase composition of the experimental alloys. Reasonable agreement between the experimental results and the phase diagrams was revealed. It was found that an addition of Al to the bcc-prone $Fe_{40}Mn_{25}Cr_{20}Ni_{15}$ alloy can result in an alloy with a high-temperature single (bcc) and a lower temperature dual (bcc+B2) phase fields.
3) Compression tests at room and elevated temperatures (25, 400, or 600 °C) have revealed that the alloys tend to become stronger with an increase in Al from 0 to 10%; further increase of Al concentration had not affected strength noticeably. The alloys exhibited pronounced softening with an increase in testing temperature from 400 °C to 600 °C. At all temperatures the alloys were highly ductile (>50%). The complex relationship between the bcc(+B2) phase(s) fraction and the yield strength of the alloys was proposed.

Acknowledgments

The authors gratefully acknowledge the financial support from the Russian Science Foundation Grant No. 18-19-00003. The authors are grateful to the personnel of the Joint Research Center, «Technology and Materials», Belgorod State University, for their assistance with the instrumental analysis.

References

[1] Y. Zhang, T.T. Zuo, Z. Tang, M.C. Gao, K.A. Dahmen, P.K. Liaw, Z.P. Lu, Microstructures and properties of high-entropy alloys, Prog. Mater. Sci. 61 (2014), https://doi.org/10.1016/j.pmatsci.2013.10.001.
[2] D.B. Miracle, O.N. Senkov, A critical review of high entropy alloys and related concepts, Acta Mater. 122 (2017) 448–511, https://doi.org/10.1016/j.actamat.2016.08.081.
[3] W. Zhang, P.K. Liaw, Y. Zhang, Science and technology in high-entropy alloys, Sci. China Mater. 61 (2018) 2–22, https://doi.org/10.1007/s40843-017-9195-8.
[4] J.-W. Yeh, S.-K. Chen, S.-J. Lin, J.-Y. Gan, T.-S. Chin, T.-T. Shun, C.-H. Tsau, S.-Y. Chang, Nanostructured high-entropy alloys with multiple principal elements: novel alloy design concepts and outcomes, Adv. Eng. Mater. 6 (2004) 299–303, https://doi.org/10.1002/adem.200300567.
[5] S. Gorsse, D.B. Miracle, O.N. Senkov, Mapping the world of complex concentrated alloys, Acta Mater. 135 (2017) 177–187, https://doi.org/10.1016/j.actamat.2017.06.027.
[6] B. Gludovatz, A. Hohenwarter, D. Catoor, E.H. Chang, E.P. George, R.O. Ritchie, A fracture-resistant high-entropy alloy for cryogenic applications, Science (80-.) 345 (2014) 1153–1158, https://doi.org/10.1126/science.1254581.

[7] B. Gludovatz, A. Hohenwarter, K.V.S. Thurston, H. Bei, Z. Wu, E.P. George, R.O. Ritchie, Exceptional damage-tolerance of a medium-entropy alloy CrCoNi at cryogenic temperatures, Nat. Commun. (2016), https://doi.org/10.1038/ncomms10602.
[8] D. Li, Y. Zhang, The ultrahigh charpy impact toughness of forged AlxCoCrFeNi high entropy alloys at room and cryogenic temperatures, Intermetallics 70 (2016) 24–28, https://doi.org/10.1016/j.intermet.2015.11.002.
[9] M.-H. Chuang, M.-H. Tsai, W.-R. Wang, S.-J. Lin, J.-W. Yeh, Microstructure and wear behavior of AlxCo1.5CrFeNi1.5Tiy high-entropy alloys, Acta Mater. 59 (2011) 6308–6317, https://doi.org/10.1016/j.actamat.2011.06.041.
[10] Y. Zou, H. Ma, R. Spolenak, Ultrastrong ductile and stable high-entropy alloys at small scales, Nat. Commun. 6 (2015), https://doi.org/10.1038/ncomms8748.
[11] Z. Li, K.G. Pradeep, Y. Deng, D. Raabe, C.C. Tasan, Metastable high-entropy dual-phase alloys overcome the strength–ductility trade-off, Nature 534 (2016), https://doi.org/10.1038/nature17981.
[12] Z. Li, C.C. Tasan, H. Springer, B. Gault, D. Raabe, Interstitial atoms enable joint twinning and transformation induced plasticity in strong and ductile high-entropy alloys, Sci. Rep. 7 (2017) 40704, https://doi.org/10.1038/srep40704.
[13] O.N. Senkov, C. Woodward, D.B. Miracle, Microstructure and properties of aluminum-containing refractory high-entropy alloys, JOM 66 (2014) 2030–2042, https://doi.org/10.1007/s11837-014-1066-0.
[14] O.N. Senkov, S.V. Senkova, C.F. Woodward, Effect of aluminum on the microstructure and properties of two refractory high-entropy alloys, Acta Mater. 68 (2014) 214–228, https://doi.org/10.1016/j.actamat.2014.01.029.
[15] O.N. Senkov, G.B. Wilks, D.B. Miracle, C.P. Chuang, P.K. Liaw, Refractory high-entropy alloys, Intermetallics 18 (2010) 1758–1765, https://doi.org/10.1016/j.intermet.2010.05.014.
[16] N.Y. Yurchenko, N.D. Stepanov, D.G. Shaysultanov, M.A. Tikhonovsky, G.A. Salishchev, Effect of Al content on structure and mechanical properties of the $Al_xCrNbTiVZr$ (x = 0; 0.25; 0.5; 1) high-entropy alloys, Mater. Char. (2016), https://doi.org/10.1016/j.matchar.2016.09.039.
[17] N.D. Stepanov, D.G. Shaysultanov, G.A. Salishchev, M.A. Tikhonovsky, Structure and mechanical properties of a light-weight AlNbTiV high entropy alloy, Mater. Lett. 142 (2015) 153–155, https://doi.org/10.1016/j.matlet.2014.11.162.
[18] N.Y. Yurchenko, N.D. Stepanov, S.V. Zherebtsov, M.A. Tikhonovsky, G.A. Salishchev, Structure and mechanical properties of B2 ordered refractory AlNbTiVZrx (x = 0–1.5) high-entropy alloys, Mater. Sci. Eng. A. 704 (2017) 82–90, https://doi.org/10.1016/j.msea.2017.08.019.
[19] H.W. Yao, J.W. Qiao, M.C. Gao, J.A. Hawk, S.G. Ma, H.F. Zhou, Y. Zhang, NbTaV-(Ti,W) refractory high-entropy alloys: experiments and modeling, Mater. Sci. Eng. A. 674 (2016) 203–211, https://doi.org/10.1016/J.MSEA.2016.07.102.
[20] D.B. Miracle, Critical Assessment 14: high entropy alloys and their development as structural materials, Mater. Sci. Technol. 31 (2015) 1142–1147, https://doi.org/10.1179/1743284714Y.0000000749.
[21] D.B. Miracle, J.D. Miller, O.N. Senkov, C. Woodward, M.D. Uchic, J. Tiley, Exploration and development of high entropy alloys for structural applications, Entropy 16 (2014) 494–525, https://doi.org/10.3390/e16010494.
[22] O.N. Senkov, J.D. Miller, D.B. Miracle, C. Woodward, Accelerated exploration of multi-principal element alloys with solid solution phases, Nat. Commun. 6 (2015) 6529, https://doi.org/10.1038/ncomms7529.
[23] W.H. Liu, T. Yang, C.T. Liu, Precipitation hardening in CoCrFeNi-based high entropy alloys, Mater. Chem. Phys. (2017), https://doi.org/10.1016/j.matchemphys.2017.07.037.
[24] J.Y. He, H. Wang, Y. Wu, X.J. Liu, H.H. Mao, T.G. Nieh, Z.P. Lu, Precipitation behavior and its effects on tensile properties of FeCoNiCr high-entropy alloys, Intermetallics 79 (2016) 41–52, https://doi.org/10.1016/j.intermet.2016.09.005.
[25] J.Y. He, H. Wang, Y. Wu, X.J. Liu, T.G. Nieh, Z.P. Lu, High-temperature plastic flow of a precipitation-hardened FeCoNiCr high entropy alloy, Mater. Sci. Eng. A. 686 (2017) 34–40, https://doi.org/10.1016/j.msea.2017.01.027.
[26] B. Gwalani, V. Soni, M. Lee, S. Mantri, Y. Ren, R. Banerjee, Optimizing the coupled effects of Hall-Petch and precipitation strengthening in a Al0.3CoCrFeNi high entropy alloy, Mater. Des. 121 (2017) 254–260, https://doi.org/10.1016/j.matdes.2017.02.072.
[27] N.D. Stepanov, N.Y. Yurchenko, M.A. Tikhonovsky, G.A. Salishchev, Effect of carbon content and annealing on structure and hardness of the CoCrFeNiMn-based high entropy alloys, J. Alloys Compd. 687 (2016) 59–71, https://doi.org/10.1016/j.jallcom.2016.06.103.
[28] J.Y. He, H. Wang, H.L. Huang, X.D. Xu, M.W. Chen, Y. Wu, X.J. Liu, T.G. Nieh, K. An, Z.P. Lu, A precipitation-hardened high-entropy alloy with outstanding tensile properties, Acta Mater. 102 (2016) 187–196, https://doi.org/10.1016/j.actamat.2015.08.076.
[29] N.D. Stepanov, N.Y. Yurchenko, S.V. Zherebtsov, M.A. Tikhonovsky, G.A. Salishchev, Aging behavior of the HfNbTaTiZr high entropy alloy, Mater. Lett. 211 (2017) 87–90, https://doi.org/10.1016/j.matlet.2017.09.094.
[30] O.N. Senkov, J.M. Scott, S.V. Senkova, D.B. Miracle, C.F. Woodward, Microstructure and room temperature properties of a high-entropy TaNbHfZrTi alloy, J. Alloys Compd. 509 (2011) 6043–6048, https://doi.org/10.1016/j.jallcom.2011.02.171.
[31] O.N. Senkov, S.L. Semiatin, Microstructure and properties of a refractory high-entropy alloy after cold working, J. Alloys Compd. 649 (2015) 1110–1123, https://doi.org/10.1016/j.jallcom.2015.07.209.
[32] Z. Tang, M.C. Gao, H. Diao, T. Yang, J. Liu, T. Zuo, Y.Y. Zhang, Z. Lu, Y. Cheng, Y.Y. Zhang, K.A. Dahmen, P.K. Liaw, T. Egami, Aluminum alloying effects on lattice types, microstructures, and mechanical behavior of high-entropy alloys systems, JOM 65 (2013) 1848–1858, https://doi.org/10.1007/s11837-013-0776-z.
[33] W.-R.W.-L. Wang, W.-R.W.-L. Wang, S.-C. Wang, Y.-C. Tsai, C.-H. Lai, J.-W. Yeh, Effects of Al addition on the microstructure and mechanical property of AlxCoCrFeNi high-entropy alloys, Intermetallics 26 (2012) 44–51, https://doi.org/10.1016/j.intermet.2012.03.005.
[34] K. Jasiewicz, J. Cieslak, S. Kaprzyk, J. Tobola, Relative crystal stability of AlxFeNiCrCo high entropy alloys from XRD analysis and formation energy calculation, J. Alloys Compd. 648 (2015) 307–312, https://doi.org/10.1016/j.jallcom.2015.06.260.
[35] S.T. Chen, W.Y. Tang, Y.F. Kuo, S.Y. Chen, C.H. Tsau, T.T. Shun, J.W. Yeh, Microstructure and properties of age-hardenable AlxCrFe1.5MnNi0.5 alloys, Mater. Sci. Eng. A. 527 (2010) 5818–5825, https://doi.org/10.1016/j.msea.2010.05.052.
[36] J.C. Rao, H.Y. Diao, V. Ocelík, D. Vainchtein, C. Zhang, C. Kuo, Z. Tang, W. Guo, J.D. Poplawsky, Y. Zhou, P.K. Liaw, J.T.M. De Hosson, Secondary phases in AlxCoCrFeNi high-entropy alloys: an in-situ TEM heating study and thermodynamic appraisal, Acta Mater. 131 (2017), https://doi.org/10.1016/j.actamat.2017.03.066.
[37] J.C. Rao, V. Ocelík, D. Vainchtein, Z. Tang, P.K. Liaw, J.T.M. De Hosson, The fcc-bcc crystallographic orientation relationship in AlxCoCrFeNi high-entropy alloys, Mater. Lett. 176 (2016), https://doi.org/10.1016/j.matlet.2016.04.086.
[38] W.R. Wang, W.L. Wang, J.W. Yeh, Phases, microstructure and mechanical properties of AlxCoCrFeNi high-entropy alloys at elevated temperatures, J. Alloys Compd. 589 (2014), https://doi.org/10.1016/j.jallcom.2013.11.084.
[39] Y. Ma, B. Jiang, C. Li, Q. Wang, C. Dong, P. Liaw, F. Xu, L. Sun, The BCC/B2 morphologies in AlxNiCoFeCr high-entropy alloys, Metals (Basel). 7 (2017) 57, https://doi.org/10.3390/met7020057.
[40] Y.F. Kao, T.J. Chen, S.K. Chen, J.W. Yeh, Microstructure and mechanical property of as-cast, -homogenized, and -deformed AlxCoCrFeNi ($0 \leq x \leq 2$) high-entropy alloys, J. Alloys Compd. 488 (2009) 57–64, https://doi.org/10.1016/j.jallcom.2009.08.090.
[41] T. Yang, S. Xia, S.S. Liu, C. Wang, S.S. Liu, Y. Zhang, J. Xue, S. Yan, Y. Wang, Effects of AL addition on microstructure and mechanical properties of AlxCoCrFeNi High-entropy alloy, Mater. Sci. Eng. A. 648 (2015) 15–22, https://doi.org/10.1016/j.msea.2015.09.034.
[42] D. Choudhuri, B. Gwalani, S. Gorsse, C.V. Mikler, R.V. Ramanujan, M.A. Gibson, R. Banerjee, Change in the primary solidification phase from fcc to bcc-based B2 in high entropy or complex concentrated alloys, Scr. Mater. 127 (2017), https://doi.org/10.1016/j.scriptamat.2016.09.023.
[43] J.Y. He, W.H. Liu, H. Wang, Y. Wu, X.J. Liu, T.G. Nieh, Z.P. Lu, Effects of Al addition on structural evolution and tensile properties of the FeCoNiCrMn high-entropy alloy system, Acta Mater. 62 (2014) 105–113, https://doi.org/10.1016/j.actamat.2013.09.037.
[44] D.G. Shaysultanov, G.A. Salishchev, Y.V. Ivanisenko, S.V. Zherebtsov, M.A. Tikhonovsky, N.D. Stepanov, Novel Fe36Mn21Cr18Ni15Al10high entropy alloy with bcc/B2 dual-phase structure, J. Alloys Compd. 705 (2017) 756–763, https://doi.org/10.1016/j.jallcom.2017.02.211.
[45] Q. Wang, Y. Ma, B. Jiang, X. Li, Y. Shi, C. Dong, P.K. Liaw, A cuboidal B2 nanoprecipitation-enhanced body-centered-cubic alloy Al0.7CoCrFe2Ni with prominent tensile properties, Scr. Mater. 120 (2016) 85–89, https://doi.org/10.1016/j.scriptamat.2016.04.014.
[46] Y. Ma, Q. Wang, B.B. Jiang, C.L. Li, J.M. Hao, X.N. Li, C. Dong, T.G. Nieh, Controlled formation of coherent cuboidal nanoprecipitates in body-centered cubic high-entropy alloys based on Al 2 (Ni,Co,Fe,Cr) 14 compositions, Acta Mater. 147 (2018) 213–225, https://doi.org/10.1016/j.actamat.2018.01.050.
[47] Y. Zhou, X. Jin, L. Zhang, X. Du, B. Li, A hierarchical nanostructured Fe 34 Cr 34 Ni 14 Al 14 Co 4 high-entropy alloy with good compressive mechanical properties, Mater. Sci. Eng. A (2018), https://doi.org/10.1016/j.msea.2018.01.034.
[48] R. Feng, M.C. Gao, C. Zhang, W. Guo, J.D. Poplawsky, F. Zhang, J.A. Hawk, J.C. Neuefeind, Y. Ren, P.K. Liaw, Phase stability and transformation in a light-weight high-entropy alloy, Acta Mater. (2018), https://doi.org/10.1016/j.actamat.2017.12.061.
[49] M. Li, J. Gazquez, A. Borisevich, R. Mishra, K.M. Flores, Evaluation of microstructure and mechanical property variations in AlxCoCrFeNi high entropy alloys produced by a high-throughput laser deposition method, Intermetallics 95 (2018) 110–118, https://doi.org/10.1016/j.intermet.2018.01.021.
[50] E.J. Pickering, R. Muñoz-Moreno, H.J. Stone, N.G. Jones, Precipitation in the equiatomic high-entropy alloy CrMnFeCoNi, Scr. Mater. 113 (2016), https://doi.org/10.1016/j.scriptamat.2015.10.025.
[51] N.D. Stepanov, D.G. Shaysultanov, M.S. Ozerov, S.V. Zherebtsov, G.A. Salishchev, Second phase formation in the CoCrFeNiMn high entropy alloy after recrystallization annealing, Mater. Lett. 185 (2016) 1–4, https://doi.org/10.1016/j.matlet.2016.08.088.
[52] S. Guo, C. Ng, J. Lu, C.T. Liu, Effect of valence electron concentration on stability of fcc or bcc phase in high entropy alloys, J. Appl. Phys. 109 (2011), 103505, https://doi.org/10.1063/1.3587228.
[53] M.C. Troparevsky, J.R. Morris, P.R.C. Kent, A.R. Lupini, G.M. Stocks, Criteria for predicting the formation of single-phase high-entropy alloys, Phys. Rev. X. 5 (2015), https://doi.org/10.1103/PhysRevX.5.011041.
[54] G.A. Salishchev, M.A. Tikhonovsky, D.G. Shaysultanov, N.D. Stepanov, A.V. Kuznetsov, I.V. Kolodiy, A.S. Tortika, O.N. Senkov, Effect of Mn and v on structure and mechanical properties of high-entropy alloys based on CoCrFeNi

system, J. Alloys Compd. 591 (2014) 11–21, https://doi.org/10.1016/j.jallcom.2013.12.210.
[55] Z. Sun, G. Song, J. Ilavsky, P.K. Liaw, Duplex precipitates and their effects on the room-temperature fracture behaviour of a NiAl-strengthened ferritic alloy, Mater. Res. Lett. 3 (2015) 128–134, https://doi.org/10.1080/21663831.2015.1021492.
[56] C.-J. Tong, Y.-L. Chen, J.-W. Yeh, S.-J. Lin, S.-K. Chen, T.-T. Shun, C.-H. Tsau, S.-Y. Chang, Microstructure characterization of Al x CoCrCuFeNi high-entropy alloy system with multiprincipal elements, Metall. Mater. Trans. A. 36 (2005) 881–893, https://doi.org/10.1007/s11661-005-0283-0.
[57] O. Sherby, Factors affecting the high temperature strength of polcyrystalline solids, Acta Metall. 10 (1962) 135–147, https://doi.org/10.1016/0001-6160(62)90058-5.
[58] C.-J. Tong, M.-R. Chen, J.-W. Yeh, S.-J. Lin, S.-K. Chen, T.-T. Shun, S.-Y. Chang, Mechanical performance of the Al x CoCrCuFeNi high-entropy alloy system with multiprincipal elements, Metall. Mater. Trans. A. 36 (2005) 1263–1271, https://doi.org/10.1007/s11661-005-0218-9.